# Quantifying transport within a two-cell microdroplet induced by circular and sharp channel bends

Sanjeeva Balasuriya[1]

*School of Mathematical Sciences, University of Adelaide, Adelaide SA 5005, Australia* [a)]

A passive method for obtaining good mixing within microdroplets is to introduce curves in the boundaries of the microchannels in which they flow. This article develops a method which quantifies the role of piecewise circular or straight channel boundaries on the transport within a two-cell microdroplet. Transport between the two cells is quantified as an easily computable time-varying flux, which quantifies how lobes intrude from one cell to the other as the droplet traverses the channel. The computation requires neither numerically solving unsteady boundary value problems nor performing trajectory integration, thereby providing an efficient new method for investigating the role of channel geometry on intra-droplet transport.

---

[a)]Electronic mail: sanjeevabalasuriya@yahoo.com

## I.   INTRODUCTION

The potential to trap micro/nanoparticles and/or single cells within droplets[1–3] has led to an explosion of recent interest in using continuous-flow droplet-based microfluidics[4–7] for synthesis and analysis at the micron or submicron level[2,8–20]. A common method for generating microdoplets is to inject two or more reagent phases into a main channel carrying an immisible fluid (or equivalently, have them enter from side-channels); the reagents coalesce to form microdroplets[2,6,11–13,16–19,21–23] which are carried along by the carrier fluid. The generated microdroplet often has a two-cell structure as schematically shown in Fig. 1, with the upper and lower cells containing two injected fluids[2,3,21,22,24–27]. The usual intention is to get the two fluids to mix across the centre interface to promote a chemical/biological reaction. However, this interface is usually robust[7], and transport only occurs very slowly via diffusion[2,22,24].

Since channel bends can induce transport even in laminar flows[28], many researchers have studied the effect of channel disturbances or bends to promote transport within droplets[6,18,21,22,24]. A recurring theme is attempting to determine boundaries which optimise transport[21,22,24,29–32]. However, comparison between experimental devices fabricated by different laboratories is difficult owing to the diverse methods used to quantify transport[3,22,26,27,29,31,33,34]. Coupled with the expense of fabricating microfluidic devices, experimentally determining *optimal* channel designs is therefore tricky.

An alternative is to use numerical simulations, which have been used for both microdroplets and *plugs* ('*slugs*') in which the microdroplet fills out the entire width of the microchannel[22,24,32–35]. The governing equations are usually taken to be the Stokes equations, since the flow is at low Reynolds number at these tiny dimensions. In computing solutions using direct numerical simulation (DNS), boundary conditions need to be imposed at the surface of the microdroplet[36–38]—at which the interior fluid and the immiscible outer carrier fluid come in contact—and on the outer carrier fluid at the channel boundaries. Implementing these conditions depends on the particular channel geometry, a fact which is exacerbated by the *unsteadiness* of these conditions since the microdroplet is experiencing different nearby boundaries as it traverses the channel. This formidable difficulty has only been overcome in some simplified geometries in which the boundary specifications become tractable and/or when considering plugs as opposed to droplets[33,35,39,40]. One DNS which is
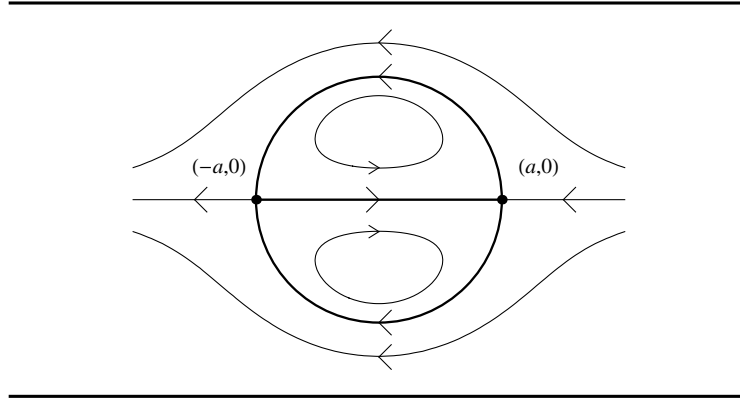
FIG. 1. Flow in droplet's frame of reference in a straight channel. The flow in the channel is from left to right in the laboratory frame, and the droplet size is exaggerated to elucidate its interior two-cell structure.

particularly related to the present article is that performed by Muradoglu and Stone[31] in a two-dimensional serpentine channel, using a finite-volume/front-tracking method (a similar computation for plugs was later developed[32]). Given the difficulty in obtaining this particular computation, a systematic way of obtaining the velocities within microdroplets resulting from *a range of* channel boundaries is impractical.

Even after the velocity field within the droplet has been determined using PIV measurements in an experiment or a DNS, a comparison of transport characteristics requires the step of quantifying mixing. A standard approach is to seed many particles, follow Lagrangian trajectories or else advect passive scalars using an advection-diffusion scheme. A norm—usually related to a variance of a concentration or intensity[3,22,26,29,31,33,34]—is then used to quantify mixing, but the fact that the norms vary between studies hinders comparison. Given this range of difficulties, using DNS to help decide what forms of channel bends are best is prohibitive.

In recognition of this, there have been many transport analyses which use simplified ordinary differential equations models intending to capture the essence of the physics[25,30,41–43]. Many build on the Hadamard-Rybczynski (HR) solution[36,37] for a spherical droplet travelling in a uniform flow field, which has symmetry about its axis; this axis consists of a heteroclinic trajectory connecting together two fixed points on the surface of the sphere. A disturbance to an HR flow, caused by an imposed time-periodic forcing[41,43], swirl[30,44], trans-

3

lational velocity[30], external strain[42] or thermocapillary effects[25], is then introduced. The velocity of the fluid—due to both the undisturbed and the disturbance physics—is thereby *specified* analytically, doing away with the need for DNS. Lagrangian particle paths still need to be computed for a range of trajectories. The generic expectation for the geometry as in Fig. 1 is that the heteroclinic trajectory which forms the interior flow interface, will split as a result of the velocity disturbance and lead to chaotic transport[45]. Not surprisingly, all these studies exhibit complicated transport[25,30,41–43].

The extension of these ideas *in quantifying the role of channel boundaries* specifically as a velocity perturbation was pursued by Stone and Stone[29]. In a specific channel comprising of a curve, a straight segment, a curve in the opposite direction, and a final straight channel, the effect of the channel curvature was modelled as an external shear flow acting on a droplet[29], a modelling hypothesis since taken up by other studies[34]. Particle trajectory simulations revealed complicated transport within the droplet, which was further analysed using a mixing norm. Detailed numerical investigations on the role of the lengths of the curved and straight segments for this *specific* channel configuration was performed at a few different values of shear flow strengths (a proxy for curvature) and viscosity ratios.

The goal of the present article is to develop a *quick* method for assessing transport due to channel geometry which is easily adaptable for *general* boundary curvature. In the spirit of similar approaches[25,29–31,41–43] this will be via a simplified model which inevitably does not capture all the physics, but which is designed specifically to elucidate the role of channel boundaries. The focus is on characterising how the transport occurs *between the upper and lower cells* of the two-cell microdroplet, as this is the instigating process for mixing between the upper and lower fluids. This shall be quantified as a time-varying function, utilising recently developed nonautonomous dynamical systems theory[46,47] (standard time-periodic analyses[48–55] are not applicable for generally varying channel boundaries).

The types of channel configurations examined in this article are illustrated in Fig. 2. Here, (a) and (b) are schematics for developing the method to curved segments and straight segments respectively; the microdroplet is shown at various points in the channel indicating that its axis is reorienting as it progresses. In (c) and (d), specific examples of curved and straight-segment serpentine channels are shown, which were chosen to conform with existing studies[18,21,22,24,26,29,31–34]. The impact of one circular bend, Fig. 2(a), is examined in Section IV, and extended to many such circular bends, Fig. 2(c), in Section V. The
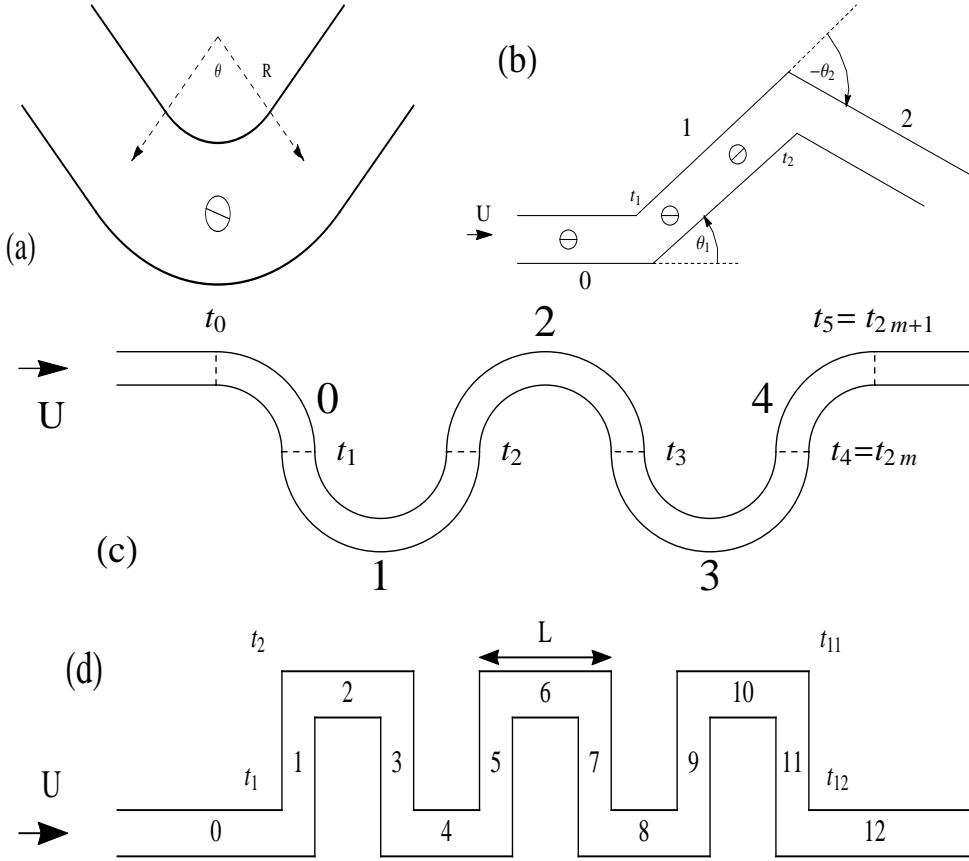
FIG. 2. Examples of channel configurations examined: (a) curved segment, (b) a curved serpentine example, (c) combinations of straight segments, and (d) serpentine channel with straight segments.

general, Fig. 2(b), and specific, Fig. 2(d), situation of connected straight channel segments is addressed in Section VI. In building up the process for determining transport in these channels, preliminary background on the HR solution for straight channels is developed in Section II, and details on how to quantify time-varying lobe-intrusion driven transport in Section III.

In all cases, explicit expressions for the transport between the cells are obtained as a function of time, which can be easily evaluated for given choices of the parameters in the system: the droplet radius, the curvature of the channel, the viscosity ratio between the droplet's interior and exterior (carrier) fluids, and the ambient flow speed along the channel. These expressions explicitly give information on the geometry and the time-variation of lobes intruding from one side to the other. Our approach allows for the quantification of transport both as an instantaneous time-dependent flux and as a cumulative volume transfer between

the cells, providing an alternative insight into the transport process from studies which mostly study the evolution of a global mixing/scattering measure[3,18,21,22,24,26,27,29–34,42,43]. As an example of the types of results which are developed, Fig. 3 shows (a) the time-varying flux from the lower to the upper cell, and (b) the accumulated volume flux by the time the droplet has gone through the bend, for the one circular bend situation of Fig. 2(a). During times of positivity of the flux function in (a), fluid from the lower cells fills out a lobe in the upper cell, and when negative the opposite happens. So one lobe of fluid from each side intrudes into the other side by the end of the process, and the areas of these lobes is shown in (b). This is the first step in achieving good mixing between the fluids; the lobes stretch and fold due to hyperbolicity and confinement, eventually filamenting to suitably small widths to allow for diffusive mixing. The variation with the curvature $1/R$ is easily assessed, and as expected, both ways of thinking about the flux decrease with $R$. As another example of the method, the time-varying flux for the square-serpentine configuration of Fig. 2(d) is shown in Fig. 4; this time, the role of different time-lags $T$ is shown. In this and in other examples, the intra-droplet flux increases with time-lag in a highly sensitive fashion. This highlights the necessity of having to carefully assess this effect in any modelling; most models impose *instantaneous* realignment[25,29,34,43,56].

Calculations such as those in Figs. 3 and 4 are easily performed using this method for any channel configuration involving connections between straight and circular channels, allowing for the ability to test for flux dependence on channel lengths and curvature, the relative viscosities of the droplet and carrier fluid, the droplet radius, and the flow rate. This therefore provides a quick method for assessing good mixing configurations, which can help choose promising designs for subsequent (more costly) analysis using experiments or DNS.

## II.   STEADY DROPLET IN AN ETCHED STRAIGHT CHANNEL

The simplest kinematical velocity distribution along the separating line which would give the behaviour shown in Fig. 1 is of the form

$$\dot{x} = k\left(a^2 - x^2\right) \quad , \quad -a \leq x \leq a \tag{1}$$

for some constant $k > 0$ which incorporates the dynamical properties of the system. While this encapsulates the geometry, a *dynamically consistent* description is necessary. Consider
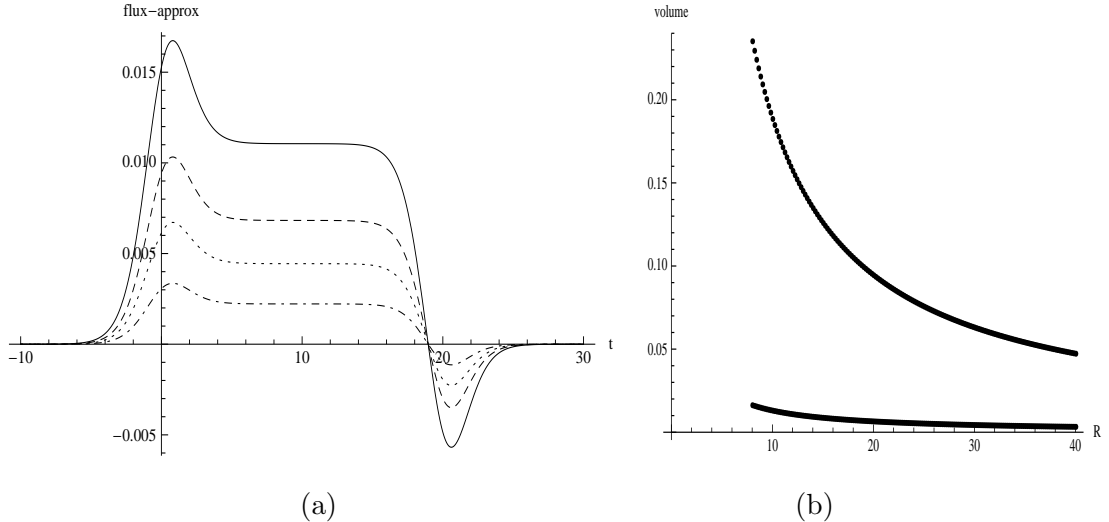
(a)　　　　　　　　　　　　　　　　(b)

FIG. 3. (a) The approximate flux for the channel configuration in Fig. 2(a), with the choices $R = 8$ (solid), $R = 13$ (dashed), $R = 20$ (dotted) and $R = 40$ (dot-dashed). (b) The total volume flux from lower to upper cell (top dots) and from upper to lower cell (bottom dots) as it varies with $R$.

the microdroplet in Fig. 1 formed by injecting two equal volumes of fluid into a channel with straight sides in which there is a steady flow of speed $U$ towards the right. Suppose the viscosity of the fluid within the droplet is $\lambda$ times the viscosity of the exterior carrier fluid. Here, the channel is considered etched on to a thin device, and thus the flow exhibits thin-film like motion which is dominantly two-dimensional. It is assumed that this two-cell droplet of radius $a$ will flow at speed $U$ in the channel while maintaining its basic structure; such is to be expected when the surface tension effects on the boundary between the two fluids counterbalances diffusion[29,36,56]. Under the assumptions of steady, low-Reynolds number flow within a uniform flow flowing to the right (in the $x$-direction in this case) at speed $U$, the velocity field in the reference frame moving with the microdropet could be modelled by

$$\dot{x} = \frac{\partial H_0}{\partial y} \quad , \quad \dot{y} = -\frac{\partial H_0}{\partial x} , \tag{2}$$

for some streamfunction $H_0(x, y)$ which satisfies the biharmonic equation for Stokes flow. The separating line between the top and bottom cells of the droplet is a heteroclinic trajectory of (2). In this two-dimensional setting (in contrast with the classical three-dimensional HR solution[29,36,37] in which the 'separating line' is surrounded by nested torii) this separator precludes transport between the upper and lower cells. Now, the heteroclinic trajectory is a solution $(\bar{x}(t), 0)$ of (2), in which $\bar{x}(t) \to -a$ and $\bar{x}(t) \to a$ as $t \to -\infty$ and $t \to \infty$
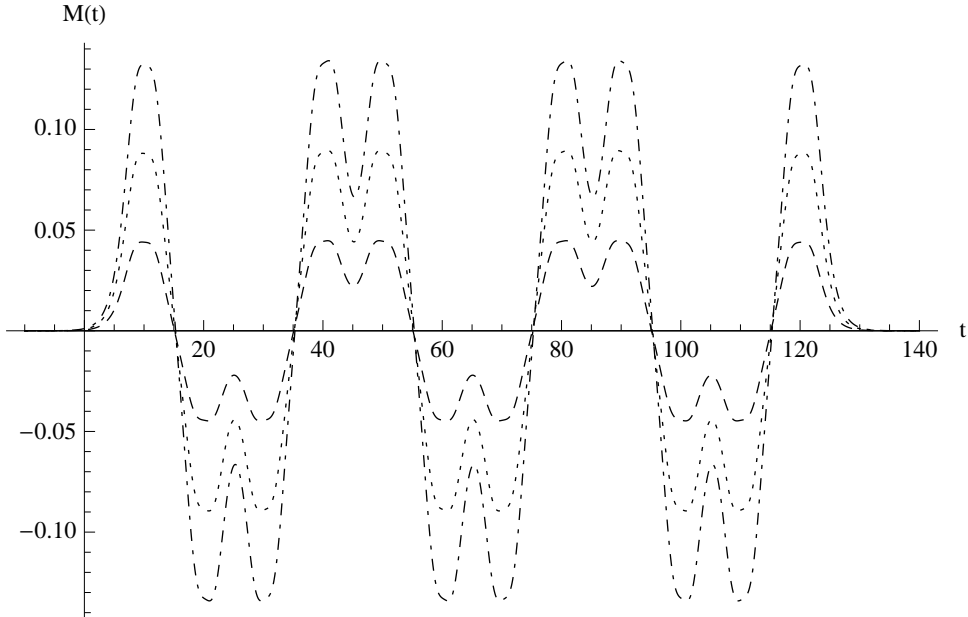
Transport in microdroplets via channel bends



FIG. 4. The flux function (32) for the square serpentine channel configuration of Fig. 2(d) with time-lags $T = 0$ (solid—along the $t$-axis), 0.2 (dashed), 0.4 (dotted) and 0.6 (dot-dashed).

respectively. Choose $\bar{x}(0) = 0$. The plan is to determine such intra-cellular flux across this separator due to the influence of the channel boundary. Our approach will be *Lagrangian* in nature, that is, it will not simply compute a flux across some fixed curve in space, which would correspond to an *Eulerian* flux which only needs the instantaneous velocity. The Lagrangian approach will take into account the motion of fluid particles, and where they come from, implicitly using information on their full trajectories.

Now, a two-dimensional realisation of the three-dimensional Hadamard-Rybczynski solution[29,36,37,56,57] would take the form

$$\dot{x} = \frac{U}{2a^2(1+\lambda)}\left(a^2 - x^2 - 3y^2\right) \quad , \quad \dot{y} = \frac{U}{a^2(1+\lambda)}xy\,, \tag{3}$$

which corresponds to a biharmonic streamfunction

$$H_0(x,y) = \frac{U}{2a^2(1+\lambda)}\left(a^2 - x^2 - y^2\right)y\,. \tag{4}$$

This is consistent with the kinematic solution (1) on the interface $y = 0$, with the choice $k = U/]2a^2(1+\lambda)]$. Hence, the $x$-coordinate variation along the separating interface is

$$\bar{x}(\tau) = a\tanh\frac{U\tau}{2a(1+\lambda)}\,, \tag{5}$$

8

with $\tau$ being used for time. Since the above expression is easily inverted, either time $\tau$ or position $\bar{x}$ can be used to parametrise the heteroclinic. At a general location $\bar{x}$ (equivalently, general parametrisation $\tau$) on the separating line, the horizontal velocity can be written as

$$u(\bar{x}) = \frac{U}{2a^2\,(1+\lambda)}\left(a^2 - \bar{x}^2\right) = \frac{U}{2\,(1+\lambda)}\mathrm{sech}^2\frac{U\tau}{2a\,(1+\lambda)} \tag{6}$$

using (3) and the fact that $d\bar{x}/d\tau = u$. The preliminary information from the *steady* flow within a droplet in a straight channel flow is now complete, and shall be the basis of computing transport between the cells when boundary curving perturbs this flow.

## III.   TRANSPORT QUANTIFICATION

Before considering the *specific* effect of channel geometry, the theory for quantifying the transport across the separating curve due to a *general* perturbation $\boldsymbol{v}(x,y,t)$, is outlined. No requirement on $\boldsymbol{v}$ being time-periodic or even smooth in time will be necessary, but $\boldsymbol{v}$ does need to be small. More details on the nonautonomous theory leading to the transport quantification outlined in this section are available elsewhere[46,47].

When $\boldsymbol{v} = \boldsymbol{0}$, the separating line $y = 0$, $-a \leq x \leq a$ in Fig. 1 separates the flow between the upper and lower cells, as pictured again in Fig. 5(a). The separating interface is a branch of the unstable manifold of the stagnation point $(-a, 0)$, and simultaneously a branch of the stable manifold of the stagnation point $(a, 0)$. Now if $\boldsymbol{v} \neq \boldsymbol{0}$ but is small, the stagnation point $(-a, 0)$ perturbs to a nearby *time-varying* entity which is called a *hyperbolic trajectory*, which continues to retain its unstable manifold, which is itself time-varying[58–60]. In Fig. 5(b), a possible situation is pictured at an instance in time. Similarly, the stable manifold of $(a, 0)$ also perturbs to a nearby entity, which is also shown in the figure. Under general $\boldsymbol{v}$, these stable and unstable manifold segments need no longer coincide. They may indeed intersect in complicated ways—at a finite or infinite number of locations—or not at all. To quantify the resulting transport at this instance in time, consider a fixed *gate-surface*[46,47,61,62] shown in gray in Fig. 5, which is a perpendicular line segment to the original separating line at the middle location $x = 0$. There is no genuine separating curve between the upper and lower cells under general splitting of the stable and unstable manifolds, which makes quantifying transport between them difficult. The solution is to define a [time-varying] *pseudoseparatrix* consisting of the unstable manifold of the perturbed version of $(-a, 0)$ until it hits the gate-surface, the stable manifold of the perturbed version of $(a, 0)$ until it hits the gate-surface,
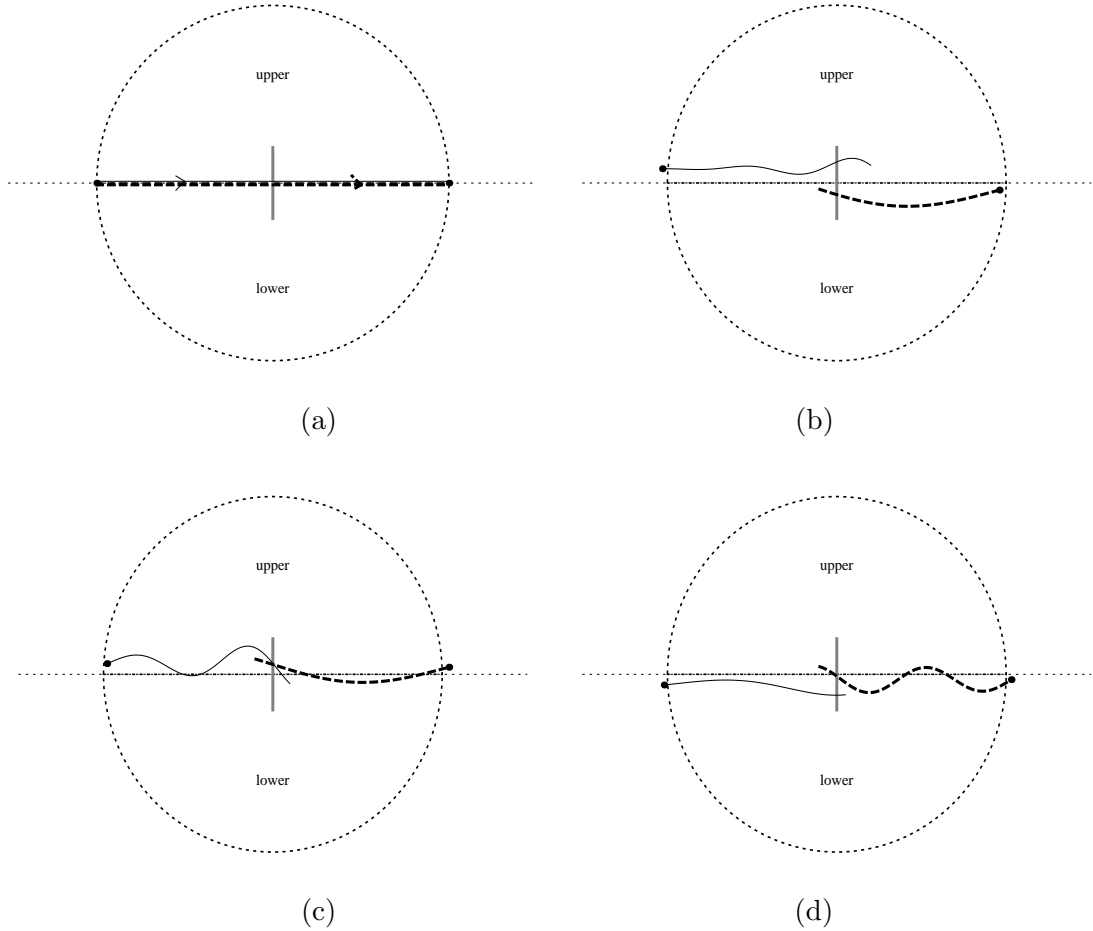
FIG. 5. (a) Stable (dashed) and unstable (solid) manifolds coincide when there is no boundary curvature. (b,c,d) Instantaneous pictures of the pertubed manifolds along with the gate-surface (gray) at times at which the flux is (b) positive, (c) zero, and (d) negative.

and the gate-surface itself. The transport across this time-varying entity is the transport occurring across the gate-surface itself, since there is no transport across the stable and unstable manifolds. In the situation pictured in Fig. 5(b), the transport across the gate-surface is from left to right. When thinking of the pseudoseparatrix as separating the upper from the lower cell, in this instance the transport is from the lower cell to the upper cell. The convention that shall be followed is that transport in the direction from the right to the left of the original flow separator (when travelling along the flow separator in the direction of the velocity) is positive. Thus *transport from the lower to the upper cell is deemed positive* in everything that follows.

Therefore, when the stable and unstable manifolds are as shown in Fig. 5(b), there is

positive transport at that instance in time. This results in fluid from the lower cell entering the upper cell as a thin filament (or elongated lobe), which elongates further due to the influence of the nearby stable manifold which attracts towards $(a, 0)$. Eventually suppose that Fig. 5(c) occurs; at this instance there is zero transport, since the stable and the unstable manifolds intersect on the gate-surface. The elongated lobe closes off. If the manifolds continuously evolve to the situation of Fig. 5(d), then there is instantaneously a negative transport. This gradually fills up an intruding lobe of fluid from the upper to the lower cell. Whenever an interchanging of relative positions along the gate-surface occurs, an elongated lobe of fluid is spat into the cell which has the *other* type of fluid. During this process, incompressibility forces the outer boundaries of the droplet to deform to adjust for the fluid volumes being exchanged within the droplet. Since the lobes are confined (the outer boundaries of the microdroplet, consisting themselves of stable and unstable manifolds, are impermeable since the outer carrier fluid is immiscible), they elongate and fold around, influenced by the exponential stretching of the manifolds. Eventually, they become sufficiently thin to be influenced by diffusion; thus, this initial transport across the pseudoseparatrix is the essential first step in achieving good mixing between the fluids of the two cells.

Quantitatively, the instantaneous transport from the lower to the upper cell, at a time $t$, to leading-order in the smallness of the perturbing unsteady velocity $\boldsymbol{v}$, can be represented by[46,47]

$$M(t) = \int_{-\infty}^{\infty} v^{\perp}\left(\bar{x}(\tau), 0, t + \tau\right) |u(\tau)| \, \mathrm{d}\tau \, . \tag{7}$$

Here, $v^{\perp}$ is the component of the perturbing velocity field $\boldsymbol{v}$ which locally is perpendicular to the separating line in the direction of transport positivity (i.e, in the $+y$-direction), and $u(\tau)$ is the unperturbed velocity along the separating line at the point $\bar{x}(\tau)$. The function $M$ is a *Melnikov function* which unlike in the classical interpretation[49,50,63] is valid for general aperiodic $\boldsymbol{v}$. The theory related to the Melnikov function has been used previously in situations in which flux is to be maximised in time-periodic flows[52–55,64]. Unlike in previous applications[47,52–55,64], the Melnikov function need not be multiplied by a small parameter since this smallness is encoded in $\boldsymbol{v}$. Thus, $M(t)$ can be thought of as the *flux function*, directly quantifying the area of fluid per unit time being transported from the lower to the

upper cell instantaneously at a general time $t$, with error $\mathcal{O}(|\boldsymbol{v}|^2)$. Since $d\bar{x}/dt = u$,

$$M(t) = \int_{\tau=-\infty}^{\infty} v^{\perp}\left(\bar{x}, 0, t+\tau\right) \mathrm{d}\bar{x}\,, \tag{8}$$

a mixed form representation which will be useful in what follows.

It must be emphasised that the Melnikov function derivation utilises the Lagrangian particle trajectories, and thereby the flux as defined in (7) is not an Eulerian flux computation. This distinction is important in unsteady flows. For example, an Eulerian computation might compute the instantaneous flux across a *fixed* curve in space, which will not take into account the fact that the curve itself would be moving as a material entity. The Lagrangian approach leading to the derivation of (7) does take this into account, while utilising the special properties of stable and unstable manifolds as important demarcators between coherent structures.

Suppose there is a range of time $[t_1, t_2]$ during which the flux $M(t)$ is positive, with the situation of Fig. 5(b) being present. This fills out a lobe of (lower) fluid which enters into the upper cell. The eventual area of this lobe, by the time it pinches off into the upper cell at $t = t_2$, is

$$V = \int_{t_1}^{t_2} M(t)\,\mathrm{d}t\,. \tag{9}$$

If $M$ switches sign in between $t_1$ and $t_2$, one can compute the corresponding lobe-area transported within each time subinterval by breaking up $[t_1, t_2]$ into subintervals within which $M$ is sign-definite ; if positive, it is from the lower to the upper cell, and if negative, it is in the opposite direction. The expression (9) generalises the lobe area interpretation as the integral of the absolute Melnikov function for time-periodic flows[48,51].

## IV.   ONE CIRCULAR BEND

Modelling transport in channels with circularly curving boundaries is fundamental to understanding more complicated boundaries[35]. Previous experimental and analytic work[29,56] indicates that the droplet realigns to make its axis locally parallel to the channel sides. Stone and Stone[29] model such a channel curvature as an added shear flow on the Hadamard-Rybczynski solution, and use numerical simulations to show that transport occurs within the droplet[29]. Here, a quantitative measure of transport which can be *explicitly* represented

as a function of time is sought, by utilising analytical methods which are able to quantify Lagrangian fluid transport from information on the Eulerian velocity field[46,47].

Consider Fig. 2(a), where the channel is straight except for one region which goes through a circular arc of radius $R$ occurring over an angle $\theta$. If the droplet enters the circular region at time $t_1$, and exits at time $t_2$, then $t_2 - t_1 = R\theta/U$. It will be assumed that

$$\varepsilon := \frac{1}{2(1+\lambda)} \frac{a}{R}$$

is a small (but not necessarily tiny) parameter. Since $a < R$ would be needed physically for the droplet to remain inside the channel, $\varepsilon$ is automatically less than $1/(2 + 2\lambda)$, which is guaranteed to be less than $1/2$. Every modelling approach so far assumes that the droplet instantaneously realigns so that its axis is parallel with the channel boundaries. However, the fact that the boundary has experienced curvature will transmit itself to the middle of the channel only after a lagged time, and hence a reasonable modification would be to assume that the droplet's orientation at some instance in time would be governed by the channel curvature at some lagged instance in time. Assume this lagged time is $T$. Based on experimental results which indicate that the droplet aligns relatively quickly to the local channel curvature, it is assumed that the time lag is short in comparison to the time within the curved channel, that is, $UT/R \ll 1$.

The assumption now is that *the velocity in the centre of the channel remains parallel to the local channel walls.* This is a caused by boundary shear[29], but only information at the center of the channel is needed for computing the leading-order flux across the interface within the microdroplet. An alternative way of stating this is that the velocity vector in this central region is perpendicular to the vector drawn to the local centre of curvature, as indicated by the thick arrow at the location $\bar{x}$ in Fig. 6. This figure shows the time-instance $t$ in a rotated reference frame drawn so the droplet is directly below the centre of curvature. The fact that there is a time-lag for realignment makes its (unperturbed) separating interface line (running from $-a$ to $a$) to be at an angle $\beta$ to the horizontal; this orientation is parallel to the boundary near where the droplet was at the time-instance $t - T$. The centre-line velocity assumption in a curved geometry means that the velocity across the interface is different at each location $\bar{x}$.

The required $v^\perp$ for using (8) is the velocity component in the direction of the dashed arrow in Fig. 6, given by $v^\perp(\bar{x}, 0, t) = u(\bar{x})\sin(\alpha + \beta)$ within the appropriate time interval.
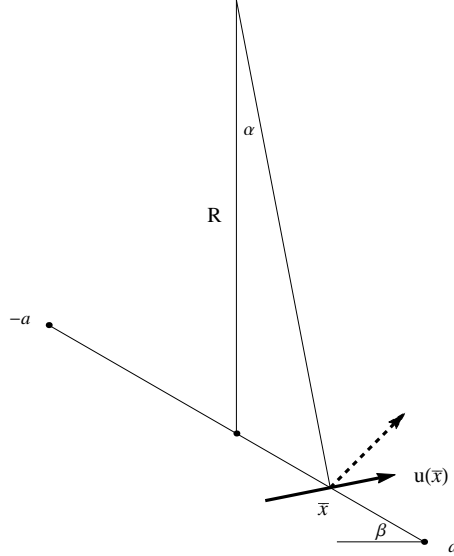
Transport in microdroplets via channel bends



FIG. 6. Computing velocity perturbation on heteroclinic due to circular undulation with lagged realignment represented by a lagged rotation angle $\beta$.

Using elementary trigonometry,

$$\sin(\alpha + \beta) = \frac{R \sin \beta + \bar{x}}{\sqrt{R^2 + (\bar{x})^2 + 2\bar{x}R \sin \beta}},$$

and therefore using (6),

$$v^\perp(\bar{x}, 0, t) = \frac{U(a^2 - \bar{x}^2)}{2a^2(1 + \lambda)} \frac{R \sin \beta + \bar{x}}{\sqrt{R^2 + \bar{x}^2 + 2\bar{x}R \sin \beta}}. \tag{10}$$

Now, the first factor on the right-hand side above is less than $U/(2(1 + \lambda))$. If $\beta = 0$, the second term is less than $a/R$, which means that $v^\perp$ is less than $\varepsilon U$, and hence can be considered a perturbation. On the other hand, ignoring the $\bar{x}$ terms leads to this second term being less than $\sin \beta \approx \beta \approx UT/R$. Thus, $v^\perp$ is small in terms of both small parameters.

The $t$-dependence in (10) is encoded in the value of $\beta$, the determination of which requires time to be divided into three segments in which there is nontrivial transport:

(i) $t_1 \leq t < t_1 + T$: the droplet maintains the orientation it had in the straight channel, while it is moving in the curved channel. In other words, the droplet does not realign.

(ii) $t_1 + T \leq t < t_2$: the droplet is in the curved channel, and its orientation is based on its position in the curved channel a time $T$ previously.

14

(iii) $t_2 \leq t < t_2 + T$: now, the droplet has left the curved channel and is in the straight channel once again, but its orientation is based on its position in the curved channel a time $T$ before that.

For $t < t_1$ and $t \geq t_2 + T$, the droplet is exactly oriented with the straight channel, and so no transport results.

In case (i), the droplet is within the curved channel, but its orientation is the same as it was in the straight channel since it had not as yet had sufficient time to adjust. Since the droplet has travelled a time $t - t_1$ within the curved channel by this point, its orientation has changed by an angle $U(t - t_1)/R$. Thus, the formula (10) is valid for $t \in [t_1, t_1 + T]$ with the replacement $\beta = U(t - t_1)/R$. Now consider case (ii), in which $t \in [t_1 + T, t_2)$. Here, the droplet would have been in the curved channel for the entire duration of the past $T$ time units, and thus $\beta = UT/R$, which is a constant. Finally, for case (iii) in which $t \in [t_2, t_2 + T)$, the droplet has left the curved channel and entered the straight channel, but its orientation is governed by its presence within the curved channel at a time $T$ previously. During this past $T$ time units, it would have travelled within the curved channel for a time $t_2 - (t - T)$, and thus $\beta = U(t_2 - t + T)/R$. Applying (10) and then replacing $t$ with $t + \tau$ as required for (8) leads to

$$M_{\text{circ}}(t) = \frac{U}{2a^2 (1 + \lambda)} \left[ I_i(t) + I_{ii}(t) + I_{iii}(t) \right] ,\tag{11}$$

where cases (i), (ii) and (iii) are encoded respectively in the expressions

$$I_i(t) := \int_{\tau = t_1 - t}^{t_1 - t + T} \frac{\left( R \sin \frac{U(t + \tau - t_1)}{R} + \bar{x} \right) (a^2 - \bar{x}^2)}{\sqrt{R^2 + \bar{x}^2 + 2R\bar{x} \sin \frac{U(t + \tau - t_1)}{R}}} \, d\bar{x} ,\tag{12}$$

$$I_{ii}(t) := \int_{\tau = t_1 - t + T}^{t_2 - t} \frac{\left( R \sin \frac{UT}{R} + \bar{x} \right) (a^2 - \bar{x}^2)}{\sqrt{R^2 + \bar{x}^2 + 2R\bar{x} \sin \frac{UT}{R}}} \, d\bar{x} ,\tag{13}$$

$$I_{iii}(t) := \int_{\tau = t_2 - t}^{t_2 - t + T} \frac{\left( R \sin \frac{U(t_2 - t - \tau + T)}{R} + \bar{x} \right) (a^2 - \bar{x}^2)}{\sqrt{R^2 + \bar{x}^2 + 2R\bar{x} \sin \frac{U(t_2 - t - \tau + T)}{R}}} \, d\bar{x} .\tag{14}$$

Now since

$$\left( a^2 - \bar{x}^2(\tau) \right) d\bar{x} = \left( a^2 - \bar{x}^2(\tau) \right) \frac{d\bar{x}}{d\tau} \, d\tau = \frac{a^2 U}{2(1 + \lambda)} \text{sech}^4 \frac{U\tau}{2a(1 + \lambda)} \, d\tau \tag{15}$$

by utilising (6), all integrals can be expressed properly in terms of $\tau$. This connection will be used in equations in later sections as well. Fig. 7 shows the full flux in (a); this is composed of the three contributions from $I_i$ (b), $I_{ii}$ (c) and $I_{iii}$ (d).
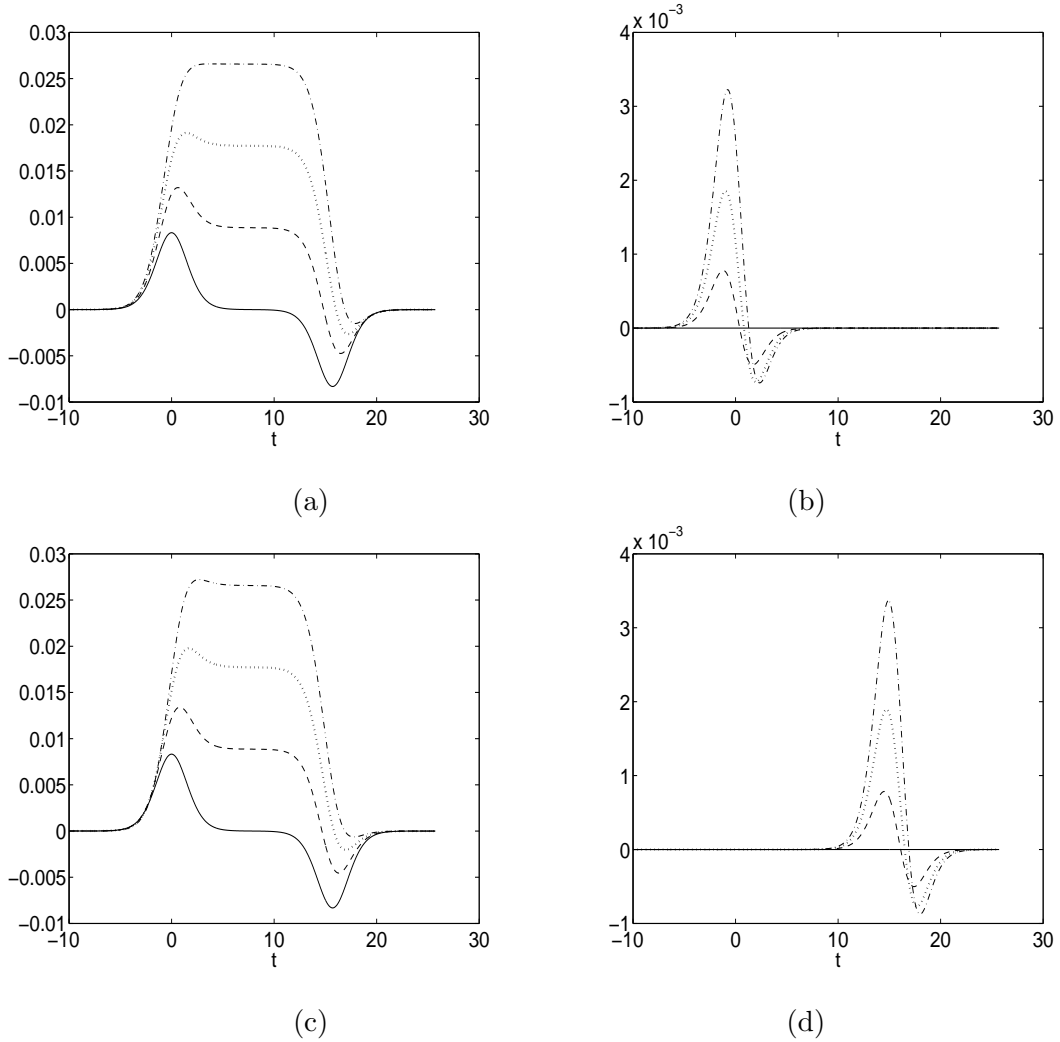
(a)



(b)



(c)



(d)

FIG. 7. (a) The flux function (11) for circular arcs with lagged droplet alignment with lags $T = 0$ (solid), 0.2 (dashed), 0.4 (dotted) and 0.6 (dot-dashed), with the parameter values $U = 1$, $a = 1$, $R = 10$, $\lambda = 0.5$, $\theta = \pi/2$, $t_1 = 0$ (and thus $t_2 = 5\pi/2$); in (b,c,d) the components resulting from cases (i), (ii) and (iii) respectively are separately plotted.

Fig. 7 indicates that the transition effects occurring in cases (i) and (iii) clearly have the most impact at respectively when the droplet is entering and exiting the curved channel, whereas the main structure of the flux function is governed by case (ii). As $T$ increases the misalignment associated with mainly case (i) (as the droplet is initially entering the curved segment) becomes significant. The solid curves in Fig. 7, corresponding to instantaneous realignment, are comparable to models such as that of Stone and Stone[29], in which an *immediate* switching of the direction of the shear stress was used to model travelling in

16

differently-curved segments of channel. Fig. 7 indicates that for such a situation of no lag time, there is first a flux upwards, and then downwards, in the microdroplet, which enhances the mixing by sloshing an elongated lobe in either direction. On the other hand, when a lag time is introduced—a situation apparently not modelled in the literature—this symmetry gradually disappears, and indeed by $T = 0.6$ the transport is essentially only in the upwards direction, and has a much larger amplitude. This amplitude indicates that more fluid is being transported at each time, while the fact that positive transport occurs over a large interval of time tells us that this results in a long lobe. Hence, increasing the lag time has the effect of increasing transport in one direction significantly, while diminishing the *exchange* of fluid between the upper and lower segments of the droplet. When there is such uni-directional flow, the enhancement of fluid *exchange* must be achieved by having a curve in the channel in the opposite direction, and a repetition of these curves leads to a serpentine channel, as investigated in the next section.

Viewing Fig. 7, the total flux (a) is seen to be approximately the same as in (c), which only includes the transport associated with $I_{ii}(t)$. This is so for any reasonable time-lag value. This is a happy circumstance, since $I_{ii}(t)$ in (13) turns out to be explicitly integrable as

$$I_{ii}(t) = R^3 \left[ \Phi \left( \frac{U(t_2 - t)}{2a(1 + \lambda)} \right) - \Phi \left( \frac{U(t_1 - t + T)}{2a(1 + \lambda)} \right) \right] \tag{16}$$

where the function $\Phi$ is defined by

$$\Phi(\xi) := \frac{1}{6} \sqrt{\left( \frac{a}{R} \right)^2 \tanh^2 \xi + 2\frac{a}{R} \sin \frac{UT}{R} \tanh \xi + 1} \left[ 1 + 3\cos \frac{2UT}{R} + 2\frac{a}{R} \sin \frac{UT}{R} \tanh \xi \right.$$
$$\left. - 2\left( \frac{a}{R} \right)^2 \tanh^2 \xi + 6\left( \frac{a}{R} \right)^2 \right]$$
$$- \sin \frac{UT}{R} \cos^2 \frac{UT}{R} \ln \left( \frac{a}{R} \tanh \xi + \sin \frac{UT}{R} + \sqrt{\left( \frac{a}{R} \right)^2 \tanh^2 \xi + 2\frac{a}{R} \sin \frac{UT}{R} \tanh \xi + 1} \right) \tag{17}$$

An analytical approximation for the flux associated with a one-bend channel is therefore

$$M_{\text{circ}}(t) \approx \frac{UR^3}{2a^2(1 + \lambda)} \left[ \Phi \left( \frac{U(t_2 - t)}{2a(1 + \lambda)} \right) - \Phi \left( \frac{U(t_1 - t + T)}{2a(1 + \lambda)} \right) \right]. \tag{18}$$

A direct comparison between the full solution (11) and the approximate solution (18) under the same conditions as Fig. 7 is shown in Fig. 8. In all the curves there is a zero of the flux function (indicating the time at which the stable and unstable manifold intersect on the gate-surface). However, when the time-lag increases, the time over which there is negative
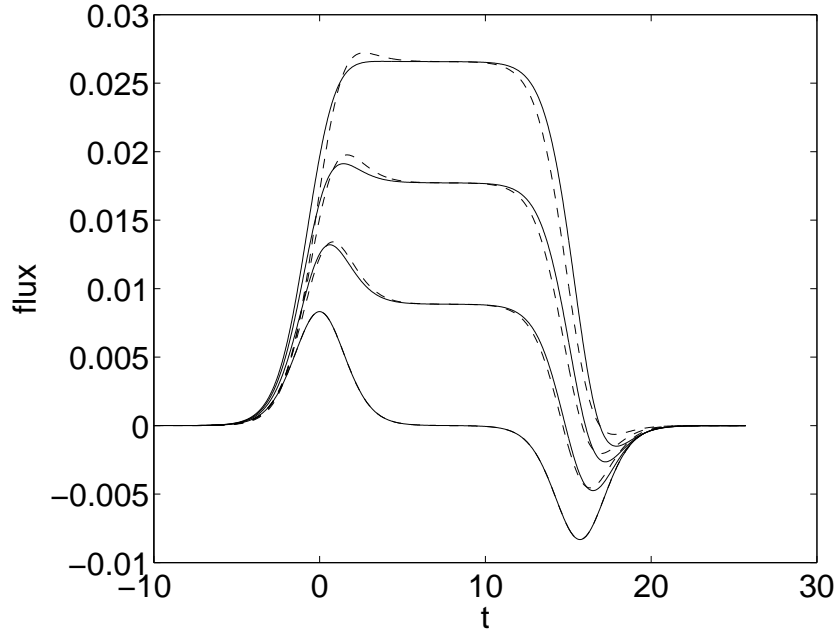
FIG. 8. A comparison between the one-circular-bend full solutions (11) (solid) and the approximate solutions (18) (dashed) with the same parameters and the four different $T$ values as in Fig. 7.

flux diminishes, and the positive flux quantity increases to quite large values. The parameter range examined in Fig. 8 corresponds to $UT/R$ going from zero to 0.06, and even in this range there is a substantial change in the flux function's behaviour. The amplitude (maximum height) of the flux function has more than tripled, and the negative flux contribution has diminished from being equal in size to the positive flux, to being about 5% of it. Thus, *the time-lag can have a significant effect on the resulting intra-droplet transport*, and is an effect which should not be ignored.

Noting that the effect of $\lambda$ within the $\Phi$ functions simply represents a time-scaling, $\lambda$'s presence in the premultiplicative factor in (18) governs the flux amplitude. Hence, smaller values of $\lambda$ give better mixing. This is entirely consistent with the observations of Stone and Stone[29] and Muradoglu and Stone[31] that smaller $\lambda$ improving mixing, which stemmed from a numerical integration of particle trajectories coupled with a backtrace imaging procedure, investigated at a few $\lambda$ values. Our model which focusses specifically on transport across the interface within the droplet captures this effect effortlessly.

In Fig. 3(a), the approximate flux function (18)'s variation with $R$ where the length of

18

the curved channel is kept fixed (the droplet enters it at $t_1 = 0$ and leaves it at $t_2 = 20$), is shown. The other parameters are $U = 1$, $a = 1$, $\lambda = 0.5$ and $T = 0.2$. The amplitude of the flux decreases with $R$. The volume of fluid transported may be a better quantifier of flux, and this, by (9), is given by the area under the curve. In particular, the volume transported from the lower to the upper cell during the duration of the process is the area under each curve in Fig. 3(a) from $-\infty$ to the point of intersection of the $t$-axis (all curves pictured approximately cross at $t = 18.96$, this closeness is since the same time-lag is used for all the curves). Similarly the volume transported in the opposite direction in the latter part of the process is [negative] the integral from 18.96 to $\infty$. The variation of these quantities with $R$, with all other parameters kept fixed, is shown in Fig. 3(b). There is rapid decay with $R$ as expected, but the decay is slower than exponential. In any case, larger $R$ leads to less transport in either direction. The asymmetry between the flux transported is much larger for smaller $R$, that is for larger curvatures, an observation which consistent with the asymmetry of the plugs observed in the DNS calculations by Che et al[35].

## V.   SERPENTINE CHANNELS WITH CIRCULAR SEGMENTS

Serpentine channels[18,21,22,24,26,29,31–34] such as those in Fig. 2(c) are a popular method of instigating fluid transport in droplets by having curved channel boundaries. Suppose there are $n$ full ($180^0$) loops, with two half ($90^0$) loops at the beginning and the end to ensure the beginning and ending parts of the channel are coaxial and in the same direction. In Fig. 2(c), $n = 3$, and it shall be assumed that $n$ is odd to ensure that the beginning and ending channels lie along a straight line. Let $n = 2m - 1$, enabling a labelling of the undulating channel segments by $0, 1, 2, \cdots, 2m$, in which channels 0 and $2m$ have half loops while the other channels have full loops. If the times at which the droplet enters and leaves the $i$th channel are respectively $t_i$ and $t_{i+1}$, then

$$t_i = t_0 + (2i - 1)\frac{R\pi}{2U} \quad \text{for } i = 1, 2, 3, \cdots, 2m \quad \text{and} \quad t_{2m+1} = t_0 + 2m\frac{R\pi}{U} . \quad (19)$$

An analysis akin to the previous section for each channel $0, 1, 2, \cdots 2m$ is necessary. For each curved segment there are two situations to consider (equivalent to cases (i) and (ii) in the previous section), corresponding to quantifying the droplet's orientation lag. Case (iii) for one segment is effectively case (i) for the subsequent segment and thus need not be

19

considered except for channel $2m$. Because of qualitatively similar behaviours within and at entry, analysis of the following channel groups is sufficient:

(a) Beginning segment of straight channel,

(b) Channel 0,

(c) Channels $1, 3, \cdots, 2m - 1$ (*odd channels*, of which there are $m$),

(d) Channels $2, 4, \cdots 2m - 2$ (*even channels*, of which there are $m - 1$),

(e) Channel $2m$, and

(f) Ending segment of straight channel.

For (a), the droplet is oriented straight and there is no boundary curvature, and thus there is no perpendicular velocity component for $t < t_0$. For (b), case (iii) from the previous section can be used, but a redrawing of Fig. 6 with the centre of curvature below rather than above the heteroclinic is neccesary. Alternatively, the concavity of the channel boundary is now negative rather than positive, and so modification of (10) is

$$v^{\perp}(\bar{x}, 0, t) = -\frac{U(a^2 - \bar{x}^2)}{2a^2(1 + \lambda)} \frac{R \sin \beta + \bar{x}}{\sqrt{R^2 + \bar{x}^2 + 2\bar{x}R \sin \beta}} ; \tag{20}$$

the negative sign results from the fact that the normal direction to the heteroclinic continues to be positive in the 'vertically upwards' direction, while the appropriate modification to Fig. 6 is obtained by reflecting it about a horizontal line. In comparison with (12) and (13) this leads to the integrals

$$I_i^b(t) = -\int_{\tau=t_0-t}^{t_0-t+T} \frac{\left(R \sin \frac{U(t+\tau-t_0)}{R} + \bar{x}\right)(a^2 - \bar{x}^2)}{\sqrt{R^2 + \bar{x}^2 + 2R\bar{x} \sin \frac{U(t+\tau-t_0)}{R}}} \, d\bar{x} , \tag{21}$$

$$I_{ii}^b(t) = -\int_{\tau=t_0-t+T}^{t_1-t} \frac{\left(R \sin \frac{UT}{R} + \bar{x}\right)(a^2 - \bar{x}^2)}{\sqrt{R^2 + \bar{x}^2 + 2R\bar{x} \sin \frac{UT}{R}}} \, d\bar{x} . \tag{22}$$

Now turn to case (c). Consider an odd channel with beginning and ending times $t_{2j-1}$ and $t_{2j}$ respectively. During the first $T$ time units within the odd channel, the droplet's orientation is influenced by its location in the previous *even* channel. The orientation difference between the current position at time $t$ and that position would be $\beta = U(t - t_{2j-1})/R - U(t_{2j-1} - (t - T))/R$, with the first term quantifying the orientation difference between the current position at time $t$ and the position of entering the current odd channel at time $t_{2j-1}$, and

the second term the difference between this position of entering the current channel and the location at time $t - T$ within the previous even channel. The negative sign results from the rotation negating the misalignment. Thus, $\beta = U(2t - 2t_{2j-1} - T)/R$, and in comparison to the results above, but now with positive concavity,

$$I_i^{c,j}(t) = \int_{\tau=t_{2j-1}-t}^{t_{2j-1}-t+T} \frac{\left(R\sin\frac{U(2t+2\tau-2t_{2j-1}-T)}{R} + \bar{x}\right)\left(a^2 - \bar{x}^2\right)}{\sqrt{R^2 + \bar{x}^2 + 2R\bar{x}\sin\frac{U(2t+2\tau-2t_{2j-1}-T)}{R}}}\,d\bar{x}\,, \tag{23}$$

$$I_{ii}^{c,j}(t) = \int_{\tau=t_{2j-1}-t+T}^{t_{2j}-t} \frac{\left(R\sin\frac{UT}{R} + \bar{x}\right)\left(a^2 - \bar{x}^2\right)}{\sqrt{R^2 + \bar{x}^2 + 2R\bar{x}\sin\frac{UT}{R}}}\,d\bar{x}\,. \tag{24}$$

Next, consider an even channel, case (d), during the time $[t_{2j}, t_{2j+1}]$. Initially the orientation is governed by the location in the previous odd channel, and this corresponds to choosing a rotation angle $\beta = U(t - t_{2j})/R - U(t_{2j} - (t - T))/R = U(2t - 2t_{2j} - T)/R$. Since these channels have negative concavity, (20) gives

$$I_i^{d,j}(t) = -\int_{\tau=t_{2j}-t}^{t_{2j}-t+T} \frac{\left(R\sin\frac{U(2t+2\tau-2t_{2j}-T)}{R} + \bar{x}\right)\left(a^2 - \bar{x}^2\right)}{\sqrt{R^2 + \bar{x}^2 + 2R\bar{x}\sin\frac{U(2t+2\tau-2t_{2j}-T)}{R}}}\,d\bar{x}\,, \tag{25}$$

$$I_{ii}^{d,j}(t) = -\int_{\tau=t_{2j}-t+T}^{t_{2j+1}-t} \frac{\left(R\sin\frac{UT}{R} + \bar{x}\right)\left(a^2 - \bar{x}^2\right)}{\sqrt{R^2 + \bar{x}^2 + 2R\bar{x}\sin\frac{UT}{R}}}\,d\bar{x}\,. \tag{26}$$

Case (e), the final curved even channel, is equivalent to case (d) with the choice $j = m$. Thus,

$$I_i^{e}(t) = -\int_{\tau=t_{2m}-t}^{t_{2m}-t+T} \frac{\left(R\sin\frac{U(2t+2\tau-2t_{2m}-T)}{R} + \bar{x}\right)\left(a^2 - \bar{x}^2\right)}{\sqrt{R^2 + \bar{x}^2 + 2R\bar{x}\sin\frac{U(2t+2\tau-2t_{2m}-T)}{R}}}\,d\bar{x}\,, \tag{27}$$

$$I_{ii}^{e}(t) = -\int_{\tau=t_{2m}-t+T}^{t_{2m+1}-t} \frac{\left(R\sin\frac{UT}{R} + \bar{x}\right)\left(a^2 - \bar{x}^2\right)}{\sqrt{R^2 + \bar{x}^2 + 2R\bar{x}\sin\frac{UT}{R}}}\,d\bar{x}\,. \tag{28}$$

Finally, when considering case (f), the droplet is now in the final straight segment of the channel. Initially its orientation is given by that of the previous even channel, i.e., equation (14), but here the concavity is negative, and so

$$I_{iii}^{f}(t) = -\int_{\tau=t_{2m+1}-t}^{t_{2m+1}-t+T} \frac{\left(R\sin\frac{U(t_{2m+1}-t-\tau+T)}{R} + \bar{x}\right)\left(a^2 - \bar{x}^2\right)}{\sqrt{R^2 + \bar{x}^2 + 2R\bar{x}\sin\frac{U(t_{2m+1}-t-\tau+T)}{R}}}\,d\bar{x} \tag{29}$$

which contributes to the integral only for $t + \tau \in [t_{2m+1}, t_{2m+1} + T]$, and there is zero contribution thereafter since the droplet would have oriented correctly to the final straight

channel. Summing all these contributions together yields the full flux function

$$M_{\text{serp}}(t) = \frac{U}{2a^2\,(1+\lambda)}\left[\left(I_i^b(t) + I_{ii}^b(t)\right) + \sum_{j=1}^{m}\left(I_i^{c,j}(t) + I_{ii}^{c,j}(t)\right)\right.$$
$$\left. + \sum_{j=1}^{m-1}\left(I_i^{d,j}(t) + I_{ii}^{d,j}(t)\right) + \left(I_i^e(t) + I_{ii}^e(t)\right) + I_{iii}^f(t)\right], \qquad (30)$$

where the definitions for the $I$s are given in (21)–(29). Given that the principal contribution to the flux comes from the '$ii$' subscripted terms, an explicit approximation for (30) would be

$$M_{\text{serp}}(t) \approx \frac{UR^3}{2a^2\,(1+\lambda)}\left[\Phi\left(\frac{U(t_0 - t + T)}{2a(1+\lambda)}\right) - \Phi\left(\frac{U(t_1 - t)}{2a(1+\lambda)}\right)\right.$$
$$+ \sum_{j=1}^{m}\left[\Phi\left(\frac{U(t_{2j} - t)}{2a(1+\lambda)}\right) - \Phi\left(\frac{U(t_{2j-1} - t + T)}{2a(1+\lambda)}\right)\right]$$
$$+ \sum_{j=1}^{m-1}\left[\Phi\left(\frac{U(t_{2j} - t + T)}{2a(1+\lambda)}\right) - \Phi\left(\frac{U(t_{2j+1} - t)}{2a(1+\lambda)}\right)\right]$$
$$\left. + \Phi\left(\frac{U(t_{2m} - t + T)}{2a(1+\lambda)}\right) - \Phi\left(\frac{U(t_{2m+1} - t)}{2a(1+\lambda)}\right)\right] \qquad (31)$$

in terms of $\Phi$ defined in (17). The approximation here is expected to be better than that for the one bend scenario since the $I_i^c$ and $I_i^d$ terms here have a smaller effect; the transition from a channel of one sign of curvature to the opposite sign means that the lag effect is diminished.

Fig. 9 shows both the flux function (30) and the approximate flux function (31) computed for the specific geometry of Fig. 2(c), i.e., with the choice $m = 2$. As in the one-bend situation, the approximate flux function provides an excellent estimate for these parameter values. As the time-lag increases, there is more transport towards the local centre of curvature in each channel segment. However, as the droplet approaches the end of each curves channel segment, there is a small amount of flux which occurs in the opposite direction. When the time-lag is zero, this amount is exactly the same as the transport towards the centre of curvature (see the solid curve in Fig. 9), but this value decreases sharply with increasing time-lag. Unlike in classical time-periodic analyses of stable and unstable manifold intersections[48–50] the sloshing back and forth does not continue indefinitely, but only happens over the time during which the droplet is travelling through the channel. Hence,
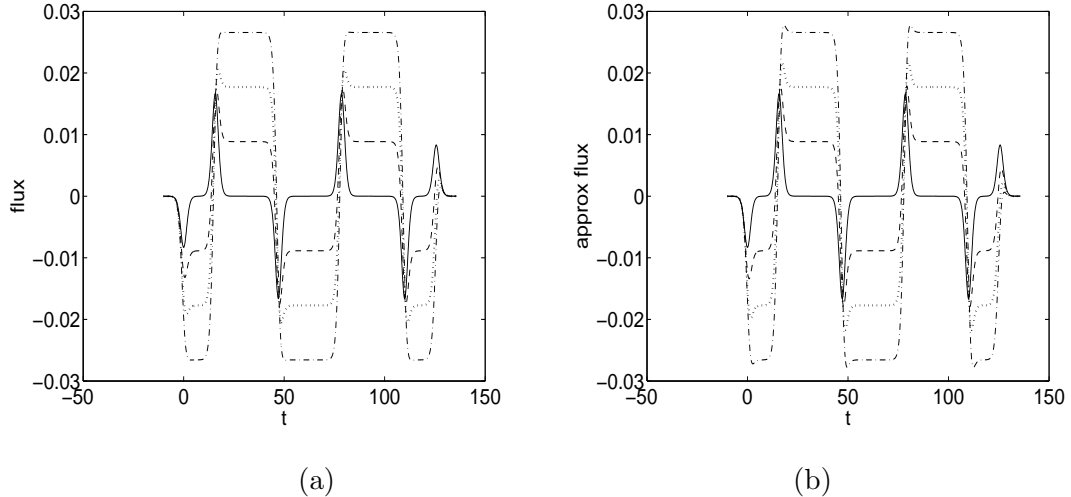
Transport in microdroplets via channel bends



FIG. 9. (a) The flux function (30) for the serpentine channel with $U = 1$, $a = 1$, $R = 10$, $\lambda = 0.5$ and $m = 2$, with lags $T = 0$ (solid), 0.2 (dashed), 0.4 (dotted) and 0.6 (dot-dashed). (b) The approximate flux function (31) under the same conditions.

the flux curves in Fig. 9 only have a finite number of intersections with the abscissa. By simply tacking on more bent segments (i.e., increasing $m$), better transport is achievable. The corresponding flux functions (not shown) are easily computable using (31) for any number of bends, and turn out to be simple extensions of Fig. 9.

The flux is a function of time. One question that might be asked is whether it is possible to come up with a specific measure of transport, which does not depend on time. An increase in transport between the upper and lower cells can be achieved when

(1) The flux function has a large size, and

(2) When the flux function changes sign often.

If only (1) occurs, then the transport would be unidirectional, but large, resulting in a large lobe intruding in one direction. If only (2) occurs but happens at small amplitude, there is back-and-forth mixing but with small lobe volumes of each fluid within the other. Neither factor by itself would lead to large 'mixing' across the flow interface. A specific measure of transport from the flux function must incorporate *both* these effects. If fully time-periodic and centred around zero, one can use the concept of an *average flux* which relates to the size of a lobe of fluid transported across per unit time[46,51–55,64]. But in our case the flux function

23

is not periodic, and indeed decays to zero as $t \to \pm\infty$ since the bending part of the channel has finite length. Such a measure is therefore not possible.

If only measuring the effect (1), one possibility would be to use an $L^1$-norm on the flux function, or something similar. If using an $L^1$-norm globally in time, information on the positive and negative aspects of the flux function disappear, and thus transport in either direction would be treated equally, and simply added together. This will therefore not be able to capture effect (2). A simple way of capturing only effect (2) would be to count the number of zeroes of the flux function. This could have difficulties when there are infinitely-many zeroes (which will not occur in this particular application), but more importantly fails to capture the amount of fluid that is being transported. Given these issues, the flux function as a function of time *without* attempting to give a time-independent measure of transport is probably the best approach. By examining its behaviour as in Fig. 9, the relevance of both effects (1) and (2) can be gleaned, retaining insight into how transport occurs with time.

## VI.   STRAIGHT CHANNEL SEGMENTS CONNECTED BY SHARP CHANNEL BENDS

Rather than using curved channels, another approach that is sometimes used is to use straight channel segments connected together by square or triangular bends[18,22,26,65]. Suppose there are $n+1$ channel segments, labelled $0, 1, 2, \cdots, n$, and the transition from the $j$th channel to the $(j + 1)$st channel occurs via an angle change of $\theta_j$, as shown in Fig. 2(b). A positive $\theta_j$ would indicate that the axis of the new channel is rotated by a counter-clockwise direction from the axis of the previous channel, whereas a negative $\theta_j$ would mean clockwise rotation. While in channel 0, the heteroclinic is exactly aligned with the channel sides, and thus there is no perpendicular component of velocity. In the initial $T$ time units while in channel 1, the orientation is the same as in channel 0, and in this case there is a perpendicular component of velocity, given by $v^\perp(x, 0, t) = u \sin \theta_1$ for $t_1 \le t < t_1 + T$ which, since there is no local boundary curvature, is the same value at all locations $x$ along the heteroclinic. While this is not small per se, its *integral over time is small* because $T$ is small (more formally, if $L$ is a scale associated with channel lengths, the requirement is that $UT/L \ll 1$). Melnikov analyses have been established to be applicable for such instances; an analysis associated with Dirac delta impulses in time, which indeed have an unbounded

24

amplitude of the 'perturbation,' is available[47]. Thus, the flux function remains legitimate. Now, for $t_1 + T \leq t < t_2$, there is no perpendicular component, since the droplet has by this stage aligned correctly. After entering channel 2, the droplet's initial alignment would be associated with channel 1, and thus $v^\perp(x, 0, t) = u \sin \theta_2$ for $t_2 \leq t < t_2 + T$. Since in Fig. 2(b), $\theta_2 < 0$, the above quantity is negative, which is the correct sign convention since velocities going from the lower to the upper cells within the droplet are considered positive. By continuing this process,

$$v^\perp(x, 0, t) = u \sin \theta_j \quad (t_j \leq t < t_j + T \quad , \quad j = 1, 2, \cdots n) ,$$

with $v^\perp = 0$ at all other times. In effect, it is only the previously subscripted '$i$' terms which contribute; the dominant '$ii$' terms obtained previously because of boundary curvature are not applicable in this situation. An immediate conclusion is straight channel boundaries offer smaller flux contributions than curved ones. Now using (8),

$$M_{\text{straight}}(t) = \sum_{j=1}^{n} \int_{\tau=t_j-t}^{t_j-t+T} u(\bar{x})) \sin \theta_j \, \mathrm{d}\bar{x}$$

$$= \frac{U}{2a^2(1+\lambda)} \sum_{j=1}^{n} \sin \theta_j \int_{\tau=t_j-t}^{t_j-t+T} \left(a^2 - \bar{x}^2\right) \, \mathrm{d}\bar{x}$$

$$= \frac{U}{2a^2(1+\lambda)} \sum_{j=1}^{n} \left[a^2\bar{x}(t_j - t + T) - \frac{\bar{x}(t_j - t + T)^3}{3} - a^2\bar{x}(t_j - t) + \frac{\bar{x}(t_j - t)^3}{3}\right] \sin \theta_j$$

$$+ \frac{1}{3}\left(\tanh^3 \frac{U(t_j - t + T)}{2a(1+\lambda)} - \tanh^3 \frac{U(t_j - t)}{2a(1+\lambda)}\right)\right] \sin \theta_j . \qquad (32)$$

The flux depends approximately linearly on the droplet radius $a$, whereas in the circular case it depended reciprocally on $a^2$ (since influenced by the curvature parameter $R$ which is absent here).

The flux function (32) is now explicitly evaluated for a configuration inspired by Fig. 2 in Tung $et$ $al$[26], which shows a planar serpentine micromixer with square bends fabricated using a micro-lithographic process. While this is serpentine-like as in Fig. 2(c), rather than having circular arcs, each rotation is achieved by using 'three sides of a rectangle.' This is shown in Fig. 2(d), with each of the shorter straight channel segments having length $L$, and here $n = 12$. Since $\theta_1 = \pi/2$, $\theta_2 = -\pi/2$, $\theta_3 = -\pi/2$, etc, $\sin \theta_j = 1$ for $j = 1, 4, 5, 8, 9, 12$ and $\sin \theta_j = -1$ for $j = 2, 3, 6, 7, 10, 11$. Moreover, $t_{j+1} = t_j + L/U$, and time will be set up such that the droplet goes through the first bend at $t = L/U$, and thus $t_j = Lj/U$.

Fig. 4 shows the flux function (32), with the choice of parameters $U = 1$, $a = 1$, $L = 10$, $\lambda = 0.5$ and $n = 12$. When $T = 0$ there is zero flux for all time, and the flux amplitude increases with $T$. For this choice of parameters, it is helpful to note that the channel bends occur at $t = 10, 20, 30, \cdots, 120$. So there is initially flux going from the lower to the upper cell, which reverses direction while the droplet is in the *middle* of channel 1. The flux is at a maximum absolute value at the instance when the droplet enters channel 2, but this amplitude decreases as it traverses channel 2. However, this amplitude increases again after the droplet passes the middle of channel 2, reaching a maximum once again at the instance of entering channel 3. Had the amplitude decrease continued, the flux would have crossed zero at an earlier instance, which would have enhanced mixing. Basically, the double-peak behaviour observed in Fig. 4 may be argued to be somewhat useless from the flux perspective; a single peak would have sufficed. The reason for the double-peak is that at $t_2$ and $t_3$, the channel bends are in the *same* direction. The insight is that had the bend at $t_3$ been in the opposite direction to what it is now, the flux function would exhibit behaviour which is more desired. From the perspective of channel design, this provides insight that a zig-zag pattern, which each bend being in the opposite direction to the previous one, is more likely to enhance intra-droplet transport.

## VII. CONCLUDING REMARKS

This article has developed a quick way for assessing transport between the cells of a microdroplet as a result of channel curvature. Unlike in experimental or DNS approaches to this problem, careful fabrication or prodigious computational costs are not required for each geometry; diverse channel configurations can be analysed with no difficulty. The approach is also much quicker than those which compute mixing for specified velocity fields, since it is not necessary to integrate thousands of Lagrangian particle trajectories. These considerable simplifications are achieved by focussing directly on the instantaneous transport occurring across the separating curve between the upper and the lower cell of the microdroplet, and utilising recent developments which enable this quantification as a time-varying quantity in systems with general time-dependence[46,47]. The effect of lag-time for the droplet to realign itself to prevailing flow conditions can also be incorporated into the development, unlike in all previous approaches. The advantage of the present simplified model is that it is able to

provide quick analyses over a range of channel configurations, and provide insight into how best to design the channels.

Transport within a four-cell microdroplet[25,30,42,44], or other similar configurations, can be analysed analogously to what has been presented in this article, with no difficulty. Thus the method is easily adaptable.

The flux functions calculated do not directly include the effects of diffusive mixing, which of course has a significant effect in any realistic situation. Given the typically low diffusion in microfluidic devices, our approach is to generate advective flow rates which (in addition to contributing to fluid transport directly) also enhance diffusive mixing through elongating the interface region between the fluids. This is accomplished by having the stable and unstable manifolds intermingle as much as possible, which is topologically identical to the graph of the flux function intersecting the $t$-axis. A realistic device with diffusion would see transport characteristics evolving in the undulating fashion of Fig. 9, superposed on the resulting diffusive mixing occurring as a result of the generated intermingling of particles. This is well illustrated in the studies by Stone and Stone[29] (with two straight and two circularly curved channels) and Muradoglu and Stones[31] (with three sinusoidal loops in their channel). In both cases, a mixing measure which quantifies how fluids from the lower and upper cells have intermingled with one another throughout the droplet is used. While a continual improvement of mixing is shown in their computed mixing measures (which inevitably includes numerical diffusion), the undulating signature of the channels is clearly present (see Fig. 7 in Stone and Stone[29] and Figures 5, 8, 11 and 14 in Muradoglu and Stone[31]). The current article analyses how one can promote the first step in this mixing—interchange of elongated lobes between the two cells—due to channel geometry. Numerical or physical diffusion will act on these lobes, leading to eventual mixing, but this is not something which can be controlled easily by modifying channel boundaries. Thus, this study obtains a quick way of quantifying *the role of channel boundaries* in causing convective transport which enhances mixing within microdroplets. Immediate insights (e.g., zig-zag configurations work better than the square bends of Fig. 2(d)) are available.

While this article focusses on straight or circular channels, transport due to *arbitrarily* curving channel boundaries is being assessed in ongoing work. A particularly interesting future topic would be whether it is possible to determine channel boundary geometries which optimise transport; previous experience in optimising fluid flux via active strategies[52–55] is

being brought to bear on this problem. Rather than having smooth transitions between channel segments, an alternative would be to have protruberances or grooves which seem intuitively at least to lead to better mixing. This too could be modelled using the present approach as *impulsive* velocity perturbations in the middle of the channel, which are amenable to a flux analysis using the integral equations approach developed by Balasuriya[47]. Optimising transport within the microdroplet may also be studied using an active strategy which controls the locations of un/stable manifolds and hyperbolic trajectories[66–69] demarcating the microdroplet, a topic of future study.

## ACKNOWLEDGMENTS

## REFERENCES

[1] A. Huebner, M. Srisa-Art, D. Holt, C. Abell, F. Hollfelder, A. deMello, and J. Edel, "Quantitative detection of protein expression in single cells using droplet microfluidics," Chem. Commum. , 1218–1220 (2007).

[2] L. Frenz, A. E. Harrack, M. Pauly, S. Bégin-Colin, D. Griffiths, and J.-C. Baret, "Droplet-based microreactors for the synthesis of magnetic iron oxide nanoparticles," Angew. Chem. Int. Ed. **47**, 6817–6820 (2008).

[3] Z. Liu, Y. Huang, Y. Jin, and Y. Chen, "Mixing intensification by chaotic advection inside droplets for controoled nanoparticle preparation," Microfluid. Nanofluid. **9**, 773–786 (2010).

[4] G. Whitesides, "The origins and future of microfluidics," Nature **442**, 368–373 (2006).

[5] A. Huebner, S. Sharma, M. Srisa-Art, F. Hollfelder, J. Edel, and A. deMello, "Micro-droplets: A sea of applications," Lab Chip **8**, 1244–1254 (2008).

[6] S.-Y. Teh, R. Lin, L.-H. Hung, and A. Lee, "Droplet microfluidics," Lab Chip **8**, 198–220 (2008).

[7] J. Atencia and D. Beebe, "Controlled microfluidic interfaces," Nature **439**, 648–655 (2005).

[8]X. Niu, F. Gielen, J. Edel, and A. deMello, "A microdroplet dilutor for high-throughput screening," Nature Chemistry **3**, 437–442 (2011).

[9]M. Bezagu, C. Enrico, V. Chaulot-Talmon, F. Monti, M. Tanter, P. Taberling, J. Cossy, S. Arseniyadis, and O. Couture, "High spatiotemporal control of spontaneous reactions using ultrasound-triggered composite droplets," J. Am. Chem. Soc. **136**, 7205–7208 (2014).

[10]L. Fidalgo, G. Whyte, B. Ruotolo, J. Benesch, F. Stengel, C. Abell, C. Robinson, and W. Huck, "Coupling microdroplet microreactors with mass spectrometry: Reading the contents of single droplets online," Angew. Chem. Int. Ed. **48**, 3665–3668 (2009).

[11]K. Seo and D. Kim, "Microfluidic synthesis of thermo-responsive poly(n-isopropylacrylamide)-poly(ethylene glycol) diacreylate microhydrogels as chemo-embolic microspheres," J. Micromech. Microeng. **24**, 085001 (2014).

[12]V. van Steijn, P. Korczyk, L. Derzsi, A. Abate, D. Weitz, and P. Garstecki, "Block-and-break generation of microdroplets with fixed volume," Biomicrofluidics **7**, 024108 (2013).

[13]N. Tarchichi, F. Chollet, and J.-F. Manceau, "New regime of droplet generation in a T-shape microfluidic junction," Microfluid. Nanofluid. **14**, 45–51 (2013).

[14]J. Boreyko, P. Mruetusatorn, S. Retterer, and C. Collier, "Aqueous two-phase microdroplets with reversible phase transitions," Lab Chip **13**, 1295–1301 (2013).

[15]M. Samie, A. Salari, and M. Shafii, "Breakup of microdroplets in asymmetric T junctions," Phys. Rev. E **87**, 053003 (2013).

[16]X. Sun, K. Tang, R. Smith, and R. Kelly, "Controlled dispensing and mixing of pico- and nanoliter volumes using on-demand droplet-based microfluidics," Microfluid. Nanofluid. **15**, 117–126 (2013).

[17]H. Zhou and S. Yao, "A facile on-demand droplet microfluidic system for lab-on-a-chip applications," Microfluid. Nanofluid. **16**, 667–675 (2014).

[18]D. Chen, C. Gerdts, and R. Ismalgilov, "Using microfluidics to observe the effect of mixing on nucleation of protein crystals," J. Am. Chem. Soc. **127**, 9672–9673 (2005).

[19]M. Hosokawa, Y. Hoshino, Y. Nishikawa, Y. Hirose, D. Yoon, T. Mori, T. Sekiguchi, S. Shoji, and H. Takeyama, "Droplet-based microfluidics for high-throughput screening of a metagenomic library for isolation of microbial enzymes," Biosensors Bioelectronics **67**, 379–385 (2015).

[20]G. Gao, E. Pfeifer, H. Farah, E. Karampini, D. Dua, N. Kamal, P. Kane, K. Tobal, T. Sethi, J. Spicer, and F. McCaughan, "Microdroplet digital pcr detection and quantitation of

biomarkers in archived tissue and serial plasma samples in patients with lung cancer," J. Thoracic Oncology **10**, 212–217 (2015).

[21]H. Song, J. Tice, and R. Ismalgilov, "A microfluidic system for controlling reaction networks in time," Angew. Chem. Int. Ed. **42**, 768–772 (2003).

[22]M. Bringer, C. Gerdts, H. Song, J. Tice, and R. Ismalgilov, "Microfluidic systems for chemical kinetics that rely on chaotic mixing in droplets," Phil. Trans. R. Soc. Lond. A **362**, 1087–1104 (2004).

[23]N. Mittal, C. Cohen, J. Bibette, and N. Bremond, "Dynamics of step-emulsification: From a single to a collection of emulsion droplet generators," Phys. Fluids **26**, 082109 (2014).

[24]H. Song, M. Bringer, J. Tice, C. Gerdts, and R. Ismalgilov, "Experimental test of scaling of mixing by chaotic advection in droplets moving through microfluidic channels," Appl. Phys. Lett. **83**, 4664–4666 (2003).

[25]R. Grigoriev, "Chaotic mixing in thermocapillary-driven microdroplets," Phys. Fluids **17**, 033601 (2005).

[26]K.-Y. Tung, C.-C. Li, and J.-T. Yang, "Mixing and hydrodynamic analysis of a droplet in a planar serpentine micromixer," Microfluid. Nanofluid. **7**, 545–557 (2009).

[27]M. Cordero, H. Rolfsnes, D. Burnham, P. Campbell, D. McGloin, and C. Baroud, "Mixing via thermocapillary generation of flow patterns inside a microfluidic drop," New J. Phys. **11**, 075033 (2009).

[28]S. Jones, O. Thomas, and H. Aref, "Chaotic advection by laminar flow in a twisted pipe," J. Fluid Mech. **209**, 335–357 (1989).

[29]Z. Stone and H. Stone, "Imaging and quantifying mixing in a model droplet micromixer," Phys. Fluids **17**, 06313 (2005).

[30]D. Kroujiline and H. Stone, "Chaotic streamlines in steady bounded three-dimensional Stokes flows," Phys. D **130**, 105–132 (1999).

[31]M. Muradoglu and H. Stone, "Mixing in a drop moving through a serpentine channel: a computational study," Phys. Fluids **17**, 073305 (2005).

[32]H. Dogan, S. Nas, and M. Muradoglu, "Mixing of mixcible liquids in gas-segmented serpentine channels," Int. J. Multiphase Flow **35**, 1149–1158 (2009).

[33]Z. Che, N.-T. Nguyen, and T. Wong, "Analysis of chaotic mixing in plugs moving in meandering microchannels," Phys. Rev. E **84**, 066309 (2011).

[34]J. Sivasamy, Z. Che, T. Wong, N.-T. Nguyen, and L. Yobas, "A simple method for

evaluating and predicting chaotic advection in microfluidic slugs," Chem. Engin. Sci. **65**, 5382–5391 (2010).

[35]Z. Che, T. Wong,  and N.-T. Nguyen, "An analytical model for a liquid plug moving in curved microchannels," Intern. J. Heat Mass Transfer **53**, 1977–1985 (2010).

[36]J. Hadamard, "Mouvement permanent lent d'une sphère liquide et visqueuse dans un liquide visqueux," C.R. Acad. Sci. Paris **152**, 1735–1738 (1911).

[37]W. Rybczynski, "Über die fortschreitende bewegung einer flüssigen kugel in einem zähen medium," Bull. Acad. Sci. Cracovi A , 40–46 (1911).

[38]S. Haber and G. Hestroni, "The dynamics of a deformable drop suspended in an unbounded Stokes flow," J. Fluid Mech. **49**, 257–277 (1971).

[39]F. Sarrazin, K. Loubière, L. Prat, C. Gourdon, T. Bonometti,  and J. Magnaudet, "Experimental and numerical study of droplet hydrodynamics in microchannels," Am. Inst. Chem. Eng. J. **52**, 4061–4070 (2006).

[40]F. Sarrazin, T. Bonometti, L. Prat, C. Gourdon,  and J. Magnaudet, "Hydrodynamic structures of droplets engineered in rectangular micro-channels," Microfluid. Nanofluid. **5**, 131–137 (2008).

[41]R. Grigoriev, M. Schatz,  and V. Sharma, "Chaotic mixing in microdroplets," Lab Chip **6**, 1369–1372 (2006).

[42]H. Stone, A. Nadim,  and S. Strogatz, "Chaotic streamlines inside drops immersed in steady Stokes flows," J. Fluid Mech. **232**, 629–646 (1991).

[43]R. Chabreyrie, D. Vainchtein, C. Chandre, P. Singh,  and N. Aubry, "Tailored mixing inside a translating droplet," Phys. Rev. E **77**, 036314 (2008).

[44]F. Wu and D. Vainchtein, "On localized mixing in action–action–angle flows," Commun. Nonlinear Sci. Numer. Simulat. **19**, 67–73 (2014).

[45]Technically speaking chaotic mixing can only be guaranteed by the Smale-Birkhoff Theorem[49] for the *homoclinic* instance where the beginning and ending saddle points are identical, *and* this homoclinic breaks up into stable and unstable manifolds which intersect infinitely many times. In this *heteroclinic* geometry the Smale-Birkhoff argument often still works if the stable and unstable manifolds are trapped and forced to return to the intersection zone.

[46]S. Balasuriya, "Nonautonomous flows as open dynamical sytems: characterising escape rates and time-varying boundaries," in *Ergodic Theory, Open Dynamics and Structures*

(Springer, 2014) Chap. 1, pp. 1–30.

[47]S. Balasuriya, "Cross-separatrix flux in time-aperiodic and time-impulsive flows," Nonlinearity **19**, 2775–2795 (2006).

[48]V. Rom-Kedar, A. Leonard, and S. Wiggins, "An analytical study of transport, mixing and chaos in an unsteady vortical flow," J. Fluid Mech. **214**, 347–394 (1990).

[49]J. Guckenheimer and P. Holmes, *Nonlinear Oscillations, Dynamical Systems and Bifurcations of Vector Fields* (Springer, New York, 1983).

[50]S. Wiggins, *Chaotic Transport in Dynamical Systems* (Springer-Verlag, New York, 1992).

[51]V. Rom-Kedar and A. C. Poje, "Universal properties of chaotic transport in the presence of diffusion," Phys. Fluids **11**, 2044–2057 (1999).

[52]S. Balasuriya, "Optimal perturbation for enhanced chaotic transport," Phys. D **202**, 155–176 (2005).

[53]S. Balasuriya, "An approach for maximizing chaotic mixing in microfluidic devices," Phys. Fluids **17**, 118103 (2005).

[54]S. Balasuriya and M. Finn, "Energy constrained transport maximization across a fluid interface," Phys. Rev. Lett. **108**, 244503 (2012).

[55]S. Balasuriya, "Optimal frequency for microfluidic mixing across a fluid interface," Phys. Rev. Lett. **105**, 064501 (2010).

[56]B. Mosovsky and J. Meiss, "Transport in transitory three-dimensional Liouville flows," SIAM J. Appl. Dyn. Sys. **11**, 1785–1816 (2012).

[57]K. Spells, "A study of circulation patterns within liquid drops moving in a liquid," Proc. Phys. Soc. Lond. B **65**, 541–546 (1952).

[58]W. Coppel, *Dichotomies in stability theory*, Lecture Notes in Math., Vol. 629 (Springer-Verlag, Berlin, 1978).

[59]Y. Yi, "A generalized integral manifold theorem," J. Differential Equations **102**, 153–187 (1993).

[60]K. Yagasaki, "Invariant manifolds and control of hyperbolic trajectories on infinite- or finite-time intervals," Dyn. Sys. **23**, 309–331 (2008).

[61]G. Haller and A. Poje, "Finite time transport in aperiodic flows," Phys. D **119**, 352–380 (1998).

[62]P. Miller, L. Pratt, K. Helfrich, and C. Jones, "Chaotic transport of mass and potential vorticity for an island recirculation," J. Phys. Oceanography **32**, 80–102 (2002).

[63]V. K. Melnikov, "On the stability of the centre for time-periodic perturbations," Trans. Moscow Math. Soc. **12**, 1–56 (1963).

[64]S. Balasuriya, "Direct chaotic flux quantification in perturbed planar flows: general time-periodicity," SIAM J. Appl. Dyn. Sys. **4**, 282–311 (2005).

[65]K. Conlisk and G. O'Connor, "Analysis of passive microfluidic mixers incorporating 2D and 3D baffle geometries fabricated using an excimer laser," Microfluid. Nanofluid. **12**, 941–951 (2012).

[66]S. Balasuriya and K. Padberg-Gehle, "Controlling the unsteady analogue of saddle stagnation points," SIAM J. Appl. Math. **73**, 1038–1057 (2013).

[67]S. Balasuriya and K. Padberg-Gehle, "Accurate control of hyperbolic trajectories in any dimension," Phys. Rev. E **90**, 032903 (2014).

[68]S. Balasuriya and K. Padberg-Gehle, "Nonautonomous control of stable and unstable manifolds in two-dimensional flows," Phys. D **276**, 48–60 (2014).

[69]S. Balasuriya, "Explicit invariant manifolds and specialised trajectories in a class of unsteady flows," Phys. Fluids **24**, 127101 (2012).